ROYAL SOCIETY OF CHEMISTRY

Check for updates

Process and design guidelines for inkjet-printed organic photovoltaic cells – using the example of PM6:Y6

Tsu-yu Chou, [ID] †[a] Tanmay Sinha, [ID] †[a] Xueshi Jiang,[b] Ekinsu Akdoğan, [ID] [a] Bernhard Siegmund, [ID] [b] Martin Rosenthal, [ID] [c] Koen Vandewal [ID] [b] and Francisco Molina-Lopez [ID] *[a]

Inkjet printing (IJP) is a promising non-contact and digital technique for the precise deposition and patterning of functional materials on reduced areas, enabling versatile applications in both indoor and outdoor environments. In this work, we present processing and design guidelines for IJP the active layer of organic photovoltaics (OPVs), covering ink preparation with non-halogenated solvents, film printing, and post-treatment. The benchmark PM6:Y6 system, a well-known high-performance donor–acceptor combination that remains relatively unexplored in the IJP field, and a commercially available IJP system are selected as a case study. Trends in power conversion efficiency (PCE) were observed with respect to the studied parameters, providing insight into the morphology–performance relationship of IJP films. Maximum optimized PCEs of 3.31% under 1 sun and 4.37% under 500 lux indoor illumination were achieved for IJP active layers produced at ambient conditions. This study highlights not only the feasibility of eco-friendly, inkjet-printed OPVs, but also general process trends to guide the fabrication of efficient, miniaturized devices for the Internet of Things (IoT), wearable electronics, and other low-power electronics applications.

1. Introduction

Photovoltaics contribute to the transition to a net-zero CO_2 emission economy by self-sufficiently driving low-power IoT applications and consumer electronics *via* exterior and interior lighting. Particularly, applications with skin contact, such as smart wearables for biomedical monitoring or portable entertainment devices such as e-readers and headphones, benefit from the biocompatibility, light weight, and mechanical flexibility[1] of organic photovoltaics (OPVs). In addition, OPVs have the advantages of solution processability, leading to low cost[2] and scalability, partial transparency,[3] low CO_2 footprint, and independence from rare earth elements.

Moreover, recent commercialization, for instance at Dracula Technologies (France) or Epishine (Sweden), underlines the commercial potential of OPVs. Especially in the last decade, the development of non-fullerene acceptors (NFAs) has pushed

the power conversion efficiency (PCE) of OPVs to more than 20%[4] enabled by the tunable bandgap and strong absorption in the NIR region by these molecules.[5,6] This flexibility in design also allows NFA-based systems to show excellent performance under indoor illumination, reaching PCEs of up to 36%.[7,8] In particular, the combination of the polymer donor poly[[2,6-(4,8-bis(5-(2-ethylhexyl)-4-fluorothiophen-2-yl)-benzo[1,2-*b*:4,5-*b'*]dithiophene))-*alt*-(5,5-(1',3'-di-2-thienyl-5',7'-bis(2-ethylhexyl)benzo[1',2'-*c*:4',5'-*c'*]dithiophene-4,8-dione))]] (PM6 or PBDB-T-2F) and the small-molecule NFA 2,2'-((2Z,2'Z)-((12,13-bis(2-ethylhexyl)-3,9-diundecyl-12,13-dihydro-[1,2,5]thiadiazolo[3,4-*e*]thieno[2'',3''':4',5']thieno[2',3':4,5]pyrrolo[3,2-*g*]thieno[2',3':4,5]thieno[3,2-*b*]indole-2,10-diyl)bis(methanylylidene))bis(5,6-difluoro-3-oxo-2,3-dihydro-1*H*-indene-2,1-diylidene))dimalononitrile (Y6 or BTP-4F) has been shown to consistently achieve PCE values over 12% under 1 sun illumination, making them the workhorse materials for the active layer of OPVs.[9–11] An important aspect to consider for IoT-based applications is patternability. Due to the limited space available on some smart devices, the lateral structuring of energy harvesters must be accurate. However, the majority of lab-scale research on OPVs is based on devices deposited by spin-coating (SC) and blade/bar-coating, which do not allow deposition in a predetermined fashion.[12] For the integration of OPVs on small devices at low cost, the technique of inkjet

[a] *Department of Materials Engineering, KU Leuven, Kasteelpark Arenberg 44, 3001 Leuven, Belgium. E-mail: francisco.molinalopez@kuleuven.be*

[b] *UHasselt, Institute for Materials Research (IMO-IMOMEC), Agoralaan, 3590 Diepenbeek, Belgium*

[c] *Department of Chemistry, KU Leuven, Celestijnenlaan 200f, 3001 Leuven, Belgium*

† Tsu-yu Chou and Tanmay Sinha have contributed equally to this work.

printing (IJP) is especially useful: it allows non-contact and digital patterning of inks without material wastage, making it suitable for minimally invasive and versatile incorporation of OPVs into the populated and quickly evolving landscape of smart wearables. Additionally, it must be noted that traditionally, OPVs have been processed with chlorinated solvents such as chloroform (CF) and chlorobenzene (CB).[9,13] These solvents are non-environment-friendly, partially undermining the low-toxicity advantage of OPVs. Hence, an effort is being made to process conjugated polymers using non-halogenated solvents, such as xylenes and tetralin,[14,15] or even more exotic terpene-based solvents.[16]

There have been a few studies demonstrating fully or partially IJP photovoltaic devices.[17–25] Despite the demonstration of functional OPVs with decent performances, a fundamental gap in understanding exists when it comes to providing general guidelines for designing and processing OPVs with IJP active layers. This lack of understanding hinders the development of IJP OPVs and their optimization for specific applications. Notably, the material system PM6:Y6, considered as a benchmark in the field of OPV due to its consistent high performance, has not been investigated in the context of IJP.

Commercial IJP technology has seen significant advancements over the past decades in terms of resolution, jetting precision, and directional stability. The popular lab-scale Fujifilm Dimatix® printer is arguably the most widespread and affordable printing equipment in the market. Their Samba® cartridge head, released in late 2021, shares the same internal jet design as industrial-scale printheads, providing the possibility of transition from laboratory to large-scale production. Yet, no studies have investigated the printability of OPV materials with this standard printing head. The fact that most reported works of IJP OPVs are based on non-commercial customized materials and printing systems sets a hard entry point to the field for researchers without synthetic chemistry expertise and creates a high barrier for translation of the technology to the market.

In this work, we provide general guidelines to produce IJP OPV active layers from non-halogenated solvents by addressing fundamental issues associated with the materials and process. As a case study, we chose the most popular and commercially available OPV material system PM6:Y6, which, despite being established as a highly performing blend, has not been investigated in the context of IJP. As printing equipment, we used the standard Fujifilm Dimatix® printer with industrial-compatible Samba® printing heads (2.4 pL droplet), which operate in ambient conditions. These settings facilitate the lab-to-fab transition, introducing a main innovation in the commercial relevance of small OPVs for the IoT.

We systematically investigated the influence of several process parameters, from ink preparation to post-treatment, on the morphology and performance of IJP OPV active layers. These parameters have been divided into the following broad categories, which define the structure of the paper: (1) ink formulation, *i.e.*, cosolvent system, and additives, (2) IJP-specific parameters, *i.e.*, jetting frequency, number of active nozzles, drop-to-drop spacing, number of printed layers (thickness), and plate temperature, and (3) post-processing, *i.e.*, annealing temperature and annealing environment. Furthermore, we investigate the influence of indoor and outdoor illumination conditions on OPV performance with an optimized IJP PM6:Y6 active layer. By comparing key performance metrics of OPVs such as open-circuit voltage (V_{oc}), short-circuit current density (J_{sc}), fill factor (FF), PCE, electron/hole mobility, series resistance (R_s) and shunt resistance (R_{sh}) for different process and design parameters, we aim to provide insights into the suitability and practical realization of IJP OPVs for energy harvesting applications.

Our findings indicate that it is important to use a cosolvent system to mitigate the coffee-ring effect. Adding a ternary high-boiling component improved phase-separation and increased the potential to reach a high maximum PCE at 1 sun, but it also enlarged the spread of the measurements, indicating a less reproducible experimental process. In addition, controlling processing conditions, such as the thickness of the printed layer and the plate temperature, proved pivotal to avoid shorting or excessive recombination, and to fine-tune crystallinity. Finally, we found vacuum thermal annealing after deposition of the active layer to be crucial to ensure complete removal of the high-boiling-point non-halogenated solvents used. While we used PM6:Y6 as a case study, our guidelines can be extended to other material systems because they address fundamental challenges related to the processing-morphology–performance relation of IJP OPVs.

2. Results and discussion

2.1. Fabrication of reference devices with spin-coated active layer

Initially, devices with active layers produced by SC, using CF as a solvent, were fabricated; first, in inert conditions, to benchmark the photovoltaic performance of our materials against reported values, and second, in ambient conditions, to act as a reference for our IJP devices. Details about the materials and processing conditions can be found in the Experimental section 4.

The chemical structures of the organic donor PM6 and NFA Y6 as well as the additive 1-chloronaphthalene (1-CN) are shown in Fig. 1a. An inverted device structure was used, with the layer stack glass (1 mm)/ITO (135 nm)/ZnO (30 nm)/PM6:Y6 (140 nm)/MoO$_3$ (14 nm)/Ag (100 nm) as shown in Fig. 1b. The active layer of the SC reference devices was fabricated both inside and outside a N$_2$-filled glovebox. Fabrication inside the glovebox was conducted to minimize the influence of moisture and oxygen, which are known to degrade device performance and reduce PCE.[26] Whilst fabrication in an inert atmosphere is the standard for OPVs, IJP operates under ambient conditions. Thus, SC reference devices were also fabricated outside the glovebox to mimic the IJP process conditions and set a fairer reference for the IJP OPV cells. The current density–voltage (J–V) curves of the reference devices are shown in Fig. 1c. While
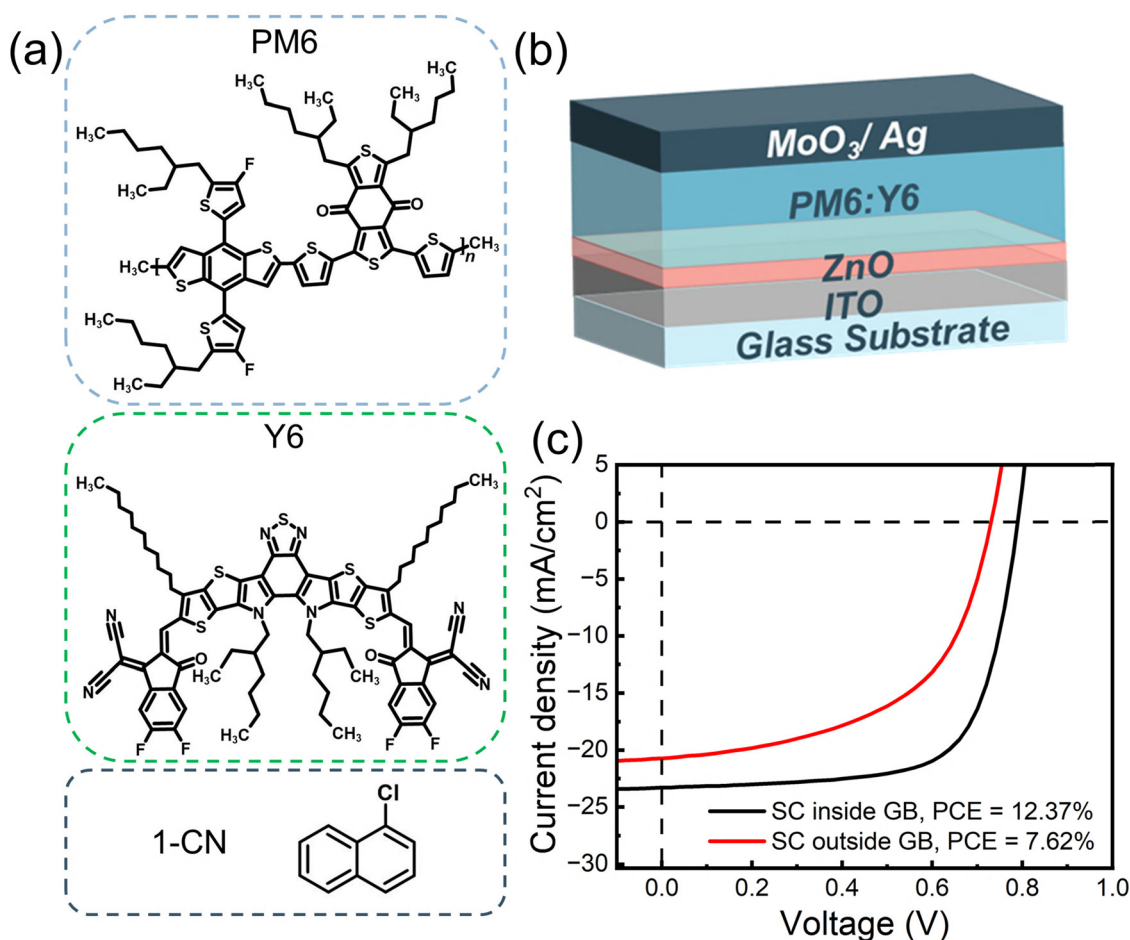
Fig. 1 Materials, device architecture, and reference devices. (a) Molecular structures of components PM6, Y6, and 1-CN. (b) Sketch of the device stacking corresponding to the inverted structure. (c) Current density–voltage (J–V) curves of a representative SC PM6:Y6 OPV fabricated inside (black) and outside (red) the glovebox (GB), showing PCE$_{avg}$ values.

the average PCE of the SC devices in CF fabricated inside the glovebox was 12.37%, consistent with values reported in literature,[9–11] the counterparts fabricated outside the glovebox displayed a comparatively lower PCE of 7.62%. This PCE reduction was likely due to environmental factors such as oxygen, moisture, and ozone, which can lead to material degradation.[27–29]

2.2. Ink formulation parameters

For IJP, a critical aspect is to choose the correct solvent(s) for processing. The selected solvent(s) must dissolve the active layer materials well and have a sufficiently high boiling point (BP) (>100 °C) to prevent nozzle clogging due to excessive solvent evaporation at the nozzle tip during printer operation. In addition, the solvent must not damage the underlayer by partially dissolving it. Keeping these aspects in mind and imposing the additional requirement of being environmentally friendly, o-xylene (BP = 144 °C) and tetralin (BP = 207 °C) were chosen for processing our inks. The choice of these solvents is further motivated by their successful use in existing literature for polymer-NFA OPVs.[30]

2.2.1. Coffee-ring effect. When using o-xylene as a single solvent, we observed the so-called coffee-ring effect, which led to uneven film thicknesses with a high root mean square (RMS) surface roughness of 50.70 nm. The coffee-ring effect takes place when the contact line of a droplet is pinned, and the difference in curvature leads to different evaporation rates between the edge and the centre of the droplet. This uneven evaporation drives a capillary flow that replenishes the evaporated solvent from the centre toward the edge, carrying solutes along and resulting in solute accumulation at the perimeter after drying.[31] In order to suppress the coffee-ring effect and achieve a more uniform active layer morphology, a cosolvent system was investigated. For this purpose, tetralin was included as a second solvent due to its good miscibility with o-xylene and high boiling point, which enhanced droplet stability and prolonged residence time in the nozzle during printing, preventing premature drying. The combination of tetralin (higher surface tension: 35.5 mN m^{-1}; and boiling point: 207 °C) with o-xylene (lower surface tension: 29.8 mN m^{-1}; and boiling point: 144 °C) effectively suppressed the formation of coffee-ring-induced edge-rich deposition patterns due to the Marangoni-enhanced
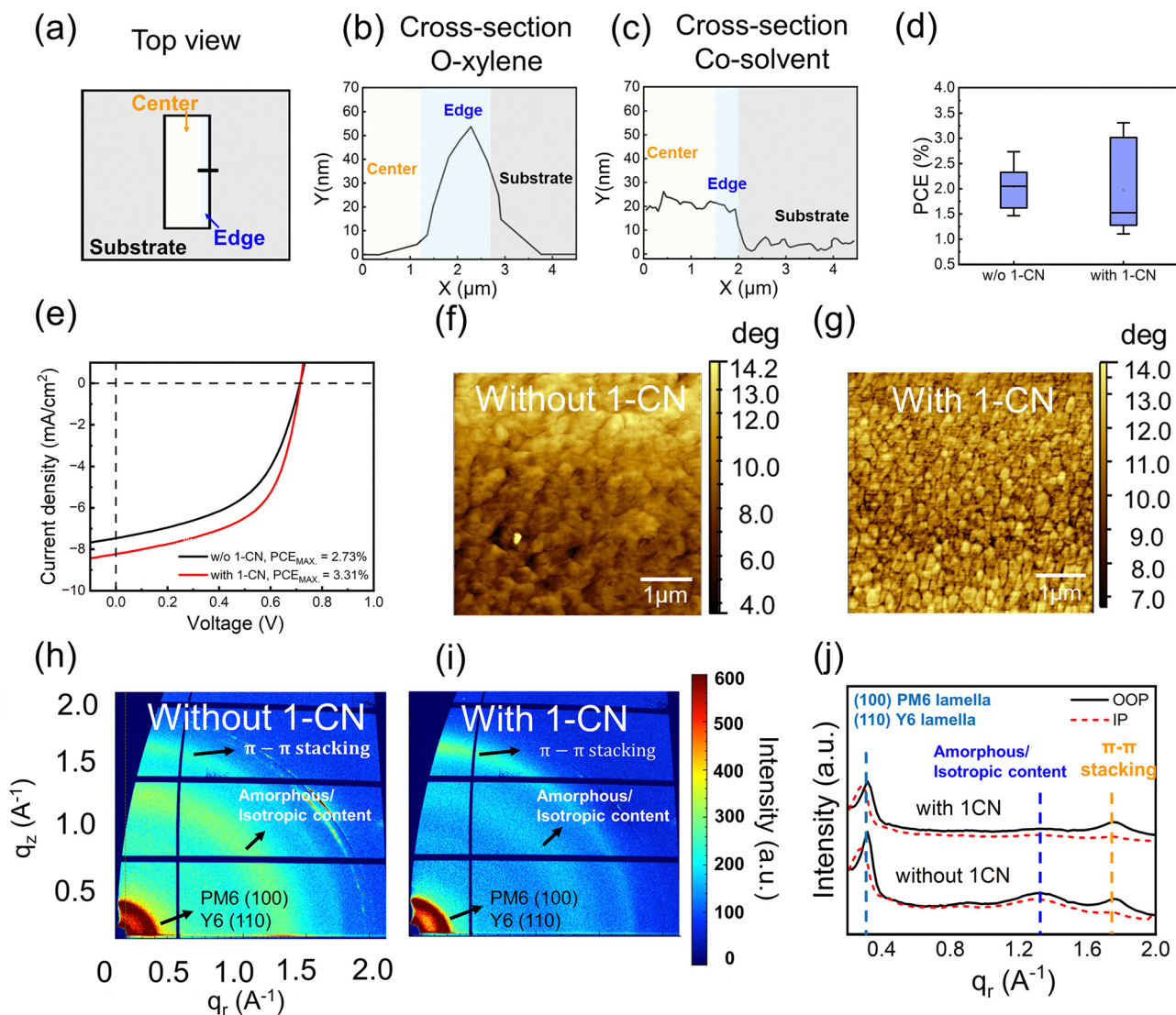
Fig. 2 Influence of ink formulation on film quality, morphology, and performance of PM6:Y6 blends. (a) Sketch of the top view of an IJP line. The black segment represents the scanning area of the AFM. The AFM-obtained cross-sectional profile of a PM6:Y6 film IJP from (b) *o*-xylene and (c) a cosolvent mixture of 95 vol% *o*-xylene and 5 vol% tetralin. (d) Box and whisker plots comparing the PCE (at 1 sun illumination) of PM6:Y6 active layers (IJP from 95:5 vol% *o*-xylene:tetralin) without and with the 1-CN additive, and (e) corresponding current density–voltage (*J*–*V*) characteristics for the top-performing cells. (f) and (g) AFM images showing phase separation in PM6:Y6 blends without and with 1-CN. (h) and (i) 2D GIWAXS patterns of PM6:Y6 films without and with 1-CN, and (j) corresponding 1D GIWAXS intensity linecuts (black solid line: out-of-plane (OOP), red dashed line: in-plane (IP)).

spreading mechanism described by Hu *et al.*[32] According to this mechanism both the capillary flow and the Marangoni flow are aligned in the same direction (towards the edge), minimizing the curvature gradient across the droplet and unpinning the contact line. Since the local curvature of the droplet influences the evaporation rate, a more uniform curvature leads to a more uniform evaporation profile, ultimately resulting in a more homogeneous film[32] with a RMS surface roughness of 17.35 nm. Fig. 2a shows the top-view schematic of an IJP line, while Fig. 2b and c present the corresponding cross-section profiles of lines deposited from single solvent (*o*-xylene) and cosolvent (*o*-xylene and tetralin) systems, respectively. In Fig. 2b, the film edge exhibited higher thickness compared to the film centre, indicating a pronounced coffee-ring effect in

single solvent systems. In contrast, incorporating a cosolvent alters the evaporation dynamics. As illustrated in Fig. 2c, the thickness variation between the centre and edge is eliminated, resulting in a much more uniform film.

2.2.2. Addition of a ternary (high-boiling) component, 1-CN. While the use of a cosolvent (95:5 vol% *o*-xylene:tetralin) system can be beneficial for eliminating the coffee-ring effect, adding a third high-boiling component can aid in separating the donor and acceptor phases, thereby improving the PCE. For the PM6:Y6 system SC from CF, 1-CN (boiling point: 259 °C) has often been used for this purpose.[9,33] The structure of 1-CN is shown in Fig. 1a.

Fig. 2d shows that adding 1-CN led to a larger spread in the PCE values (at 1 sun illumination), indicating that it introduced

variability in the experimental process. This results in similar average PCE_{avg} values (Table 2). However, IJP devices processed with 1-CN showed a higher PCE_{max} than devices processed without (3.31% vs. 2.73%, Fig. 2e), hinting at the potential of the additive to achieve higher PCE_{max} once the process can be better controlled. The positive effect of 1-CN was evidenced in the J–V characteristics of the best performing cells (Fig. 2e) by an enhancement of J_{sc} accompanied by a steeper slope near V_{oc} (but no actual change in V_{oc}),[34] which is symptomatic of a lower series resistance R_s. Indeed, a decrease in R_s (Table S1) from 4.90 Ω cm^2 to 2.05 Ω cm^2 was estimated for cells with 1-CN, signalling improved interconnectivity of domains due to a more favourable phase separation. The improved transport induced by 1-CN was also supported by the charge mobility values assessed via space-charge-limited-current (SCLC) measurements using electron-only and hole-only devices (for details, refer to the Experimental section 4). It was observed that 1-CN led to improvements in electron and hole mobilities by one order of magnitude (Table S2). It is also noteworthy that while our hole mobilities were in line with values reported in literature,[9] our best electron mobility was two orders of magnitude lower. This observation points to the fact that better PCEs might be achieved in the future by focusing on improving the acceptor morphology.

The effect of 1-CN is further confirmed by atomic force microscopy (AFM) phase images of PM6:Y6 processed without and with 1-CN (Fig. 2f and g). The RMS surface roughness for the corresponding amplitude images decreased from 17.35 nm to 7.69 nm when processing with 1-CN. More clearly defined domain boundaries and smaller domain sizes both could contribute to better charge extraction upon adding 1-CN.

To probe the effect on crystallinity of 1-CN, GIWAXS measurements were performed. Fig. 2h–j present the 2D GIWAXS data and 1D linecuts of the blend PM6:Y6 without and with 1-CN. PM6 exhibited a (100) lamellar peak at ~ 0.30 Å^{-1}, while Y6 showed a (110) lamellar peak at ~ 0.25 Å^{-1}. Both materials displayed a π–π stacking peak at ~ 1.75 Å^{-1} (Table S3 and Fig. 4c). The peak positions were in line with observations in literature.[35,36] The blend displayed a mixture of the components' features, with a merged diffraction peak around $q \sim 0.30$ Å^{-1}, corresponding to the (100) and (110) lamellar stacking of PM6 and Y6, respectively. A π–π stacking peak around $q \sim 1.75$ Å^{-1} was also observed, originating from both PM6 and (mainly) Y6. The areas under the lamellar ($q \sim 0.30$ Å^{-1}), and π–π stacking ($q \sim 1.75$ Å^{-1}) peaks or the corresponding coherence lengths did not show significant differences upon adding 1-CN (Table S4). However, a noticeable halo was present around 1.30 Å^{-1} in the blend without the additive. The origin of this feature is not clear, but halos in similar positions have been reported to come from amorphous content[35,37] or isotropic crystallinity.[38] Quantitatively, the integrated area of this halo in the in-plane (IP) and out-of-plane (OOP) directions decreased from 19.88 (a.u.) to 4.14 (a.u.) and from 22.70 (a.u.) to 6.05 (a.u.), respectively, upon addition of 1-CN (Table S4), suggesting enhanced phase separation and improved charge transport. This interpretation matches the AFM, SCLC, and max PCE results mentioned above.

Overall, the addition of 1-CN increased the potential to achieve high PCE_{max} (at 1 sun), but it also introduced dispersion in the measurements, resulting in an unchanged PCE_{avg}. These results, which contrast with the widely reported SC OPVs from CF, are unsurprising considering that the high-boiling-point solvents utilized in IJP might mask the positive effect of high-boiling-point additives.[9]

2.3. Inkjet printing specific parameters

During IJP, several parameters can be tuned to optimize film morphology.[39] Fig. 3a shows some of the key parameters: the shape of the waveform of the voltage applied to the cartridge piezo-element during jetting, the jetting frequency, the number of active nozzles, the drop-to-drop spacing (DS), the number of printed layers, and the plate temperature.

2.3.1. Waveform. Fig. 3b presents detailed information on the voltage waveform used to jet PM6:Y6 (3 mg mL^{-1}) in 95 vol% o-xylene and 5 vol% tetralin. An M-shape waveform was chosen. To prevent satellite droplets (small droplets surrounding the main droplet) and long drop tails, the amplitude and time of the different waveform parts, and the interval time between these parts must be adjusted.[40] In particular, we observed that moderately increasing the amplitude of the second part of the waveform allowed ejecting an optimal droplet for highly concentrated inks (6 mg mL^{-1}).

2.3.2. Printing frequency. Fig. S1 presents the optical images of IJP PM6:Y6 films printed from pure tetralin at different jetting frequencies on a ZnO-coated glass substrate: 5 kHz, 10 kHz, and 20 kHz. It should be noted that the experiments were carried out on ZnO, the final target surface, because the printing parameters depend on the ink-substrate interaction. Pure tetralin was chosen instead of the cosolvents due to its better jettability and longer open-nozzle time,[21] since its high boiling point of 207 °C reduced the risk of nozzle clogging during printing. Nevertheless, the results obtained for tetralin could be extended to the cosolvent system (refer to Section 2.4). The printing frequency determines the droplets' drying time before merging with subsequently deposited droplets. If the drying time is too short (high frequency), the original droplet is too wet when the new one lands; then, if wettability is poor and pinning is compromised, both droplets might merge, generating bulges in the line. On the other hand, if the droplet dries completely before the next drop lands (low frequency), the droplets do not merge well and create a 'stacked-coins' morphology.[41] Among the tested jetting frequencies, 10 kHz exhibited the best morphology. At a lower frequency (5 kHz), the film edges appeared wavy and displayed drying patterns. In contrast, at a higher frequency (20 kHz), the line definition was compromised.

2.3.3. Number of active nozzles. As a next step, we vary the number of active nozzles from 1 to 4, at the pre-optimized frequency of 10 kHz. Fig. S2 contains the fiducial camera images of IJP PM6:Y6 films printed from pure tetralin on a ZnO-coated glass substrate. For this material-substrate system, 2–3 nozzles resulted in the smoothest film boundaries. When using a single nozzle, longitudinal drying marks appeared more
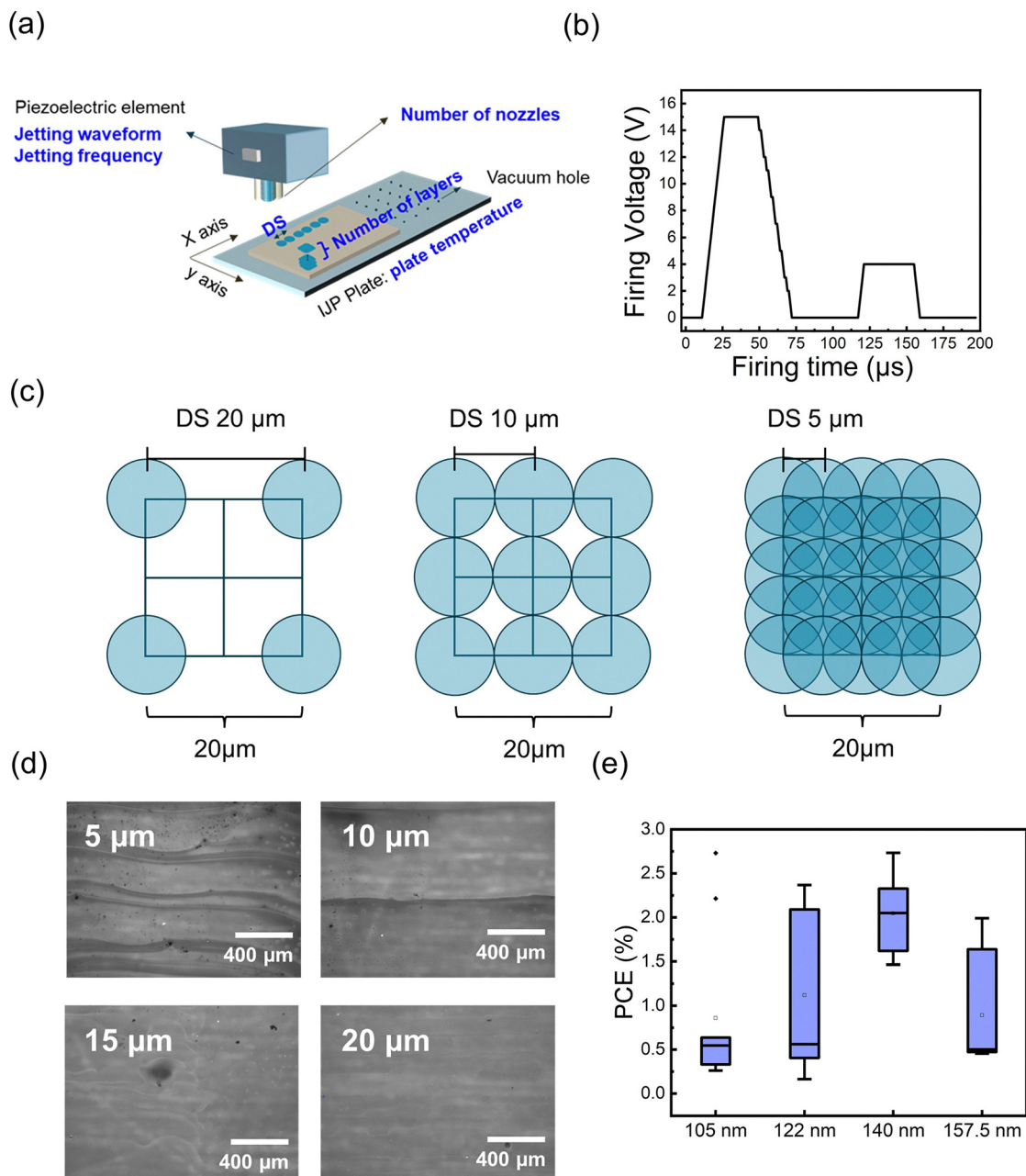
Fig. 3 Influence of IJP-specific parameters on the process-morphology–performance relationship of PM6:Y6 blends. (a) Schematic of the inkjet printer and the parameters that can be tuned. (b) Detailed information on the voltage waveform used to print PM6:Y6 in o-xylene and tetralin. (c) Schematic illustration of ink placement for different DS configurations: 20 μm, 10 μm, and 5 μm from left to right, respectively. (d) Optical images from the fiducial camera (equipped inside the Fujifilm Dimatix® 2850 inkjet printer) of PM6:Y6 films printed from tetralin with different DS ranging from 5 μm to 20 μm. (e) Box and whiskers chart comparing PCE among active layers of PM6:Y6 in tetralin with different thicknesses ranging from 105 nm to 157.5 nm. Ten devices from three different batches were characterized for optimization purposes and repeatability testing. Reported errors show the standard errors of the mean.

distinct. This may be attributed to the longer time required for the printing head to complete the same pattern with a single nozzle, since the fewer the number of nozzles, the lower the ink deposition rate. Printing slowly provides time for each line to dry before the next line is printed adjacent to it. This timing leads to an insufficient line merging manifested as drying marks that could be seen as the abovementioned 'stacked-coins' morphology for lines. On the other hand, using too

many nozzles can result in an excessive ink deposition rate, leading to over-wetting of the film (or localized ink volume exceeding the optimal drying capacity), thereby compromising film uniformity due to an uneven drying of large ink pools resulting from merged droplets. In the rest of this work, 3 nozzles were used for printing.

2.3.4. Drop-to-drop spacing. During the IJP process, droplets are deposited on the substrate using the drop-on-demand

(DoD) method, and the merging of adjacent droplets significantly influences the resulting film morphology.[42] An excessively large drop-to-drop spacing (DS) can lead to discontinuous films, whereas a DS being too small increases the likelihood of bulging, resulting in wavy and non-uniform edges. Previous reports suggest choosing the DS as approximately half the droplet diameter, as it facilitates the formation of a continuous film by proper overlapping, and yields well-aligned printed lines without liquid accumulation.[41] Fig. 3c illustrates the DS concept diagrammatically with different DS values (20 μm, 10 μm, 5 μm), while Fig. 3d shows PM6:Y6 film morphologies IJP from tetralin on ZnO-coated glass substrates, captured by the printer's fiducial camera. At DS values of 5 μm and 10 μm, excessive ink accumulation caused wavy drying patterns and uneven film formation. In contrast, films printed with DS values of 15 μm and 20 μm exhibited smoother and more uniform films. However, further increasing the DS led to discontinuous films due to insufficient droplet overlap, as can be seen in Fig. S3. For the rest of this study, a DS of 20 μm was chosen.

2.3.5. Number of printed layers (film thickness). The number of printed layers corresponds directly to the thickness of the active layer.[43] If the active layer is too thin, the risk of leakage current from one electrode to the other increases, causing a decrease in performance. If, on the other hand, the active layer is too thick, photogenerated charge carriers will recombine before reaching the electrodes. To determine the optimal number of layers and thus device thickness, we fabricated devices from 3 mg mL^{-1} ink of PM6:Y6 in o-xylene:tetralin (95:5 vol%), deposited onto an ITO/ZnO substrate (see Experimental section 4.2 for full stack). As can be seen in the box and whisker plots in Fig. 3e, printing thicknesses around 105 nm and 122 nm led to devices with relatively low PCEs with averages of 0.9 ± 0.3% and 1.1 ± 0.3%, respectively, with a large spread in measured values. Printing a thickness around 140 nm was optimum for device performance with the average PCE of 2.05 ± 0.14%, while printing even more layers decreased the PCE$_{avg}$ to 0.89 ± 0.21%.

For a deeper understanding, we modelled the J–V characteristics with a one-diode model and extracted R_s and R_{sh}[34] (see Table 1, SI1, and Table S1). The series resistance R_s refers to the internal resistance of the cell and contact resistance between different layers, whereas the shunt resistance R_{sh} represents pathways of leakage between anode and cathode and

recombination due to defects. To have a good performance for a solar cell, a low R_s and a high R_{sh} are desirable. As a benchmark, values for the reference SC samples, fabricated outside the glovebox, have been provided in Table 1. We found that thinner IJP films from around 105 nm and 122 nm (equivalent to 6 and 7 printed layers) resulted in pronounced shunts (low R_{sh}). The possible reason is that, owing to the relatively high roughness of the IJP method compared to other fabrication techniques, the insufficient film thickness leads to pinholes, causing short-circuiting paths between the two electrodes. For the thickness around 140 nm, we observed an increased R_{sh}, and when the thickness was further increased to 157.5 nm, R_{sh} stayed relatively high, supporting our hypothesis that low thickness is linked to short circuits. Meanwhile, the PCE dropped from 2.05 ± 0.14% to 0.89 ± 0.21%, as R_s gradually increased from 2.05 Ω cm^2 at the optimal thickness of 140 nm to 9.21 Ω cm^2 at a thickness of 157.5 nm. Likely, in this high-thickness regime, not all generated excitons can be separated into free charges due to the presence of isolated domains inside the active layer. Therefore, the number of printed layers in the IJP process plays a critical role in determining device performance. In this study, a film thickness of approximately 140 nm exhibited not only the highest PCE, but also the lowest standard error in device performance among the thicknesses varying from 105 nm to 157.5 nm (equivalent to IJP 6 layers to 9 layers), as observed for ten devices fabricated across three different batches. This optimised thickness is governed by achieving a balance between the values of R_s and R_{sh}: a high-enough R_{sh} to prevent shunts and R_s as low as possible.

2.3.6 Plate temperature. The temperature of the inkjet printer plate plays a key role in determining the uniformity of the active layer,[31] by affecting the solvent evaporation rate and hence polymer molecular packing and domain formation.[37] To explore the influence of different plate temperatures on film morphology, imaging with a fiducial camera and GIWAXS measurements provided complementary macroscopic and microscopic perspectives, respectively. Fig. 4a and b present images of IJP PM6:Y6 films dissolved in o-xylene:tetralin (95:5 vol%) processed under two conditions: room temperature (RT) and 60 °C. The sample processed at RT exhibited a higher degree of agglomeration compared to the one processed at 60 °C, which can be attributed to differences in drying kinetics. This macro-scale agglomeration may impact both the micro-structural morphology and the device performance.

Table 1 Series (R_s) and shunt (R_{sh}) resistances of SC and IJP PM6:Y6 OPV devices, fabricated outside the glovebox. For the reference SC condition, four devices are included, while the rest of the values represent the average of 10 devices across three different batches. Reported errors are the standard errors of the mean. PCE$_{avg}$ represents the average PCE value, and PCE$_{max}$ represents the value of the top-performing device. All measurements were performed under 1 sun illumination (AM 1.5G) for a device area of 0.04 cm^2

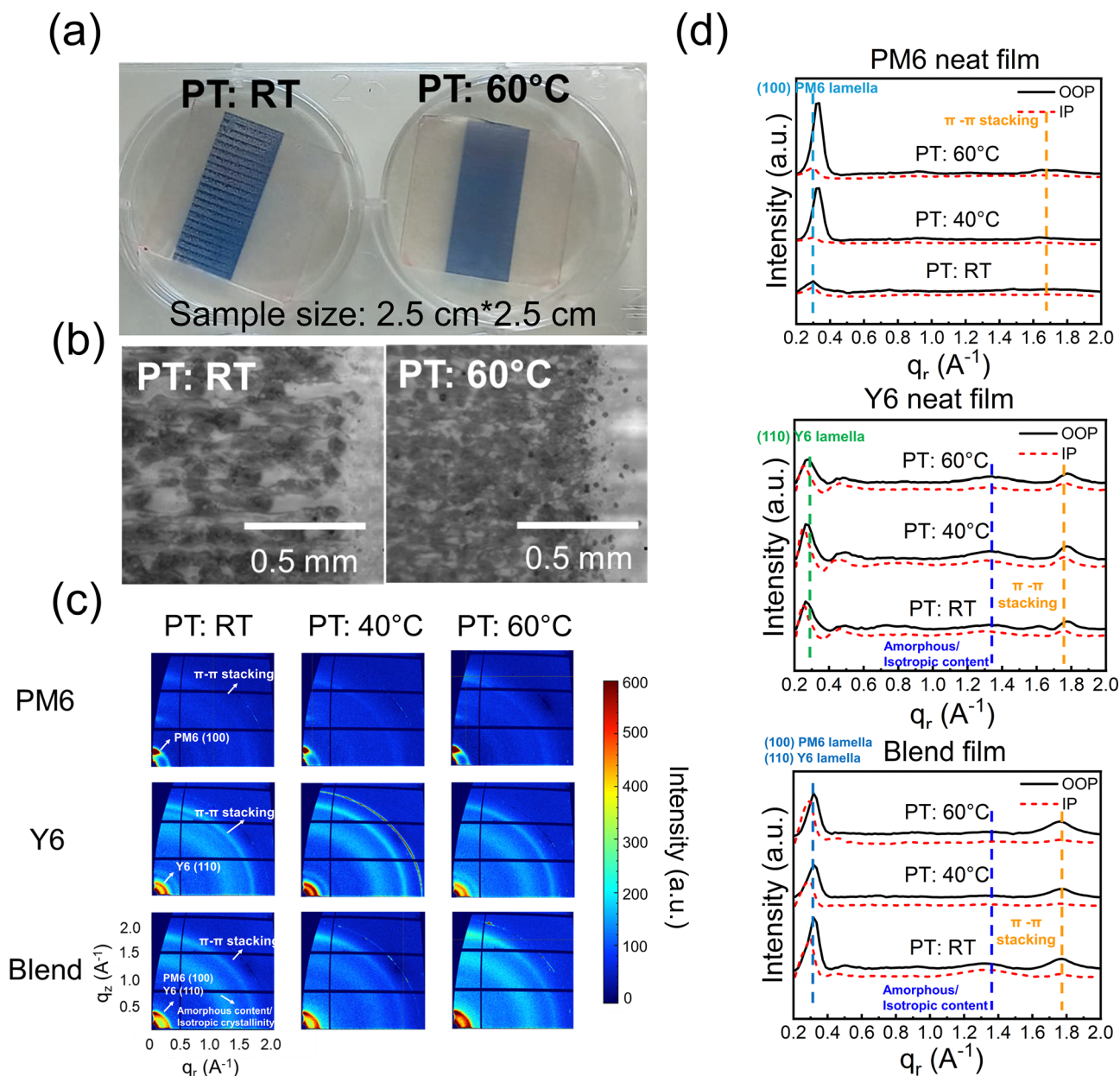| Fabrication	Thickness (nm)	Solvent	R_s (Ω cm^2)	R_{sh} (Ω cm^2)	PCE$_{avg}$ (%)	PCE$_{max}$ (%)
SC	140	Chloroform	0.87	4.69×10^8	7.62 ± 0.22	8.20
IJP	105	o-Xylene:tetralin (95:5% v/v)	51.93	7.49×10^3	0.9 ± 0.3	2.73
IJP	122	o-Xylene:tetralin (95:5% v/v)	13.26	1.20×10^3	1.1 ± 0.3	2.37
IJP	140	o-Xylene:tetralin (95:5% v/v)	4.9	4.70×10^9	2.05 ± 0.14	2.73
IJP	157.5	o-Xylene:tetralin (95:5% v/v)	9.21	2.03×10^9	0.89 ± 0.21	1.99

Fig. 4 Effect of IJP plate temperature on the morphology of PM6:Y6 films. (a) and (b) Optical images taken with the printer fiducial camera of PM6:Y6 films IJP from *o*-xylene:tetralin (95:5% v/v) under two plate temperature conditions: room temperature (RT) and 60 °C. (c) 2D GIWAXS patterns of the IJP neat films PM6, Y6, and the blend film from *o*-xylene:tetralin (95:5% v/v) on Si substrate at plate temperatures of RT, 40 °C, and 60 °C. (d) GIWAXS 1D intensity linecuts for the films in panel (c).

Consequently, a comprehensive investigation of changes in the crystalline structures of materials at different plate temperatures was carried out.

Fig. 4c and d present the 2D GIWAXS patterns and 1D linecuts of the blend PM6:Y6 films as well as the neat films of PM6 and Y6 IJP from *o*-xylene:tetralin (95:5 vol%) on a Si substrate at plate temperatures of RT, 40 °C, and 60 °C. The diffractograms reveal key features of the active layer materials (Table S3): PM6 exhibited a mostly OOP (100) lamellar peak at ~ 0.30 Å^{-1} and a faint π–π stacking feature at ~ 1.70 Å^{-1}, while Y6 showed a relatively isotropic (110) lamellar peak at approximately 0.25 Å^{-1} and a clear π–π stacking peak at 1.70 Å^{-1}. As

discussed before, the peak at around 1.3–1.4 Å^{-1} may be representative of the existence of an amorphous region or isotropic crystallinity. From the 1D linecuts for PM6 in the OOP direction, it may be inferred that the lamellar and π–π stackings in PM6 strengthened with increasing plate temperature. The lamellar peak at ~ 0.3 Å^{-1} showed an increase in crystalline coherence length (CCL) from 56.13 Å to 82.80 Å as the plate temperature was raised from RT to 60 °C, while the area under this peak increased from 18.26 (a.u.) to 97.75 (a.u.) (Table S3). The π–π stacking peak at 1.7 Å^{-1} became prominent at higher plate temperatures, with the area under it increasing from 2.10 (a.u.) at RT to 9.74 (a.u.) at 60 °C. The increase in

lamella CCL and peak area, and the emergence of a π–π stacking feature, indicated strongly improved crystallinity when the plate temperature was increased. Y6 neat films featured high crystallinity even at RT, and no significant improvements were observed upon increasing the plate temperature. For the blend film, modest crystallinity improvements could mainly be seen when increasing plate temperature from RT to 60 °C in the lamella, with the corresponding CCL increasing from 65.19 Å to 74.31 Å in the IP direction and from 68.86 Å to 75.66 Å in the OOP direction. Following the discussion above, these improvements in the blend may be attributed primarily to better packing among PM6 molecules. Compared to neat PM6 films, the crystallinity improvements in the blend upon heating the printing plate were modest because they were probably attenuated by the unaltered (and high) Y6 crystallinity. This highlights an important observation: Y6, being a small molecule, can achieve a favourable crystallinity even at low plate temperatures. PM6, on the other hand, requires enhanced molecular mobility due to its larger molecular size, hence necessitating a higher plate temperature for the optimization of its molecular ordering through diffusion.

2.4. Post-processing parameters

2.4.1. Thermal annealing. Thermal annealing of the OPV active layer is an important step to ensure that the donor and acceptor separate into domains with improved molecular packing, and that efficient charge generation and separation can take place.[44] Meanwhile, an excessive annealing temperature could lead to inefficient charge extraction primarily due to demixing and suboptimal morphology,[32] or material degradation. While optimal annealing conditions are well-known for PM6:Y6 blends SC from CF, this information remains to be explored for IJP films processed with high-boiling solvents.[45]

As mentioned before, in this work, we have used a combination of o-xylene and tetralin to mitigate the coffee-ring effect. To investigate the requirements imposed on thermal annealing by such a high-boiling solvent system, we first studied the thermal annealing on films processed completely from tetralin, which is the component with the highest boiling point of 207 °C. Fig. 5a reveals an abnormal 'S-shaped' J–V curve[46–48] and a short-circuit when the tetralin-processed device was annealed for 30 minutes at 140 °C inside the glovebox. The low PCE observed was attributed to incomplete drying of the active layer film. Evidence of entrapped residual solvent in the active layer included poor film adhesion to the underlying electron-transport layer (ETL) (Fig. S5), greyish top electrode (anode) colour, and abnormally high film thickness ~0.4 μm measured versus the expected 140 nm (Fig. S6).

Given the high boiling point of tetralin, complete solvent evaporation without material degradation posed a challenge. To address this, three experimental approaches were tested (Fig. S7): (1) a second post-annealing for 20 minutes at 160 °C in the glovebox after top electrode evaporation (Fig. S8), (2) extending the post-annealing time after active layer deposition from 30 minutes to 60 minutes at 140 °C (Fig. S9), and (3)

post-annealing under vacuum after active layer deposition at 140 °C for 30 min.

Approach (1), i.e., a second annealing step at 160 °C for 20 minutes after Ag deposition, effectively eliminated the 'S-shape' anomaly. Nevertheless, the improvement in the PCE was only marginal, suggesting that residual solvent remained in the active layer and a higher annealing temperature was required. Unfortunately, further increasing the annealing temperature to 180 °C resulted in a decline in PCE, suggesting thermal degradation of the material or an unfavourable evolution of morphology. Approach (2), i.e., extending the post-annealing duration to 60 minutes at 140 °C inside the glovebox, did not improve the J–V curve, indicating that a higher annealing temperature rather than a longer annealing time is the main requirement to eliminate tetralin residue. To bypass the conflict between solvent removal and material thermal stability, we found vacuum annealing to be a promising strategy to lower the boiling point of the solvent and effectively reduce solvent residue in the active layer without degrading it. Using the Clausius–Clapeyron equation (SI2), the boiling point of tetralin was estimated to decrease to approximately 97.5 °C under the low pressure of 10 mmHg used during approach (3). The resulting shunt-free devices with a notable increase in PCE (Fig. 5b) make vacuum annealing a simple and viable method to improve the performance of IJP OPVs, which requires solvents with boiling points above the degradation temperature of the active layer materials. It is worth noting that vacuum annealing may not be ideal for traditional solution-processable OPVs, which target high-throughput, large-area, roll-to-roll manufacturing. In contrast, the goal of IJP-processed OPVs is to produce many small devices in a batch-to-batch manner. From this perspective, the process proposed in this work can still be regarded as scalable, analogous to wafer-level microelectronics fabrication, where vacuum steps such as physical vapor deposition are already well established.

To correlate our findings concerning thermal annealing with nanomorphology, the annealing conditions mentioned above were replicated for film crystallinity measurements using GIWAXS. The 2D GIWAXS patterns of PM6:Y6 processed in pure tetralin, along with their corresponding 1D linecuts, are shown in Fig. 5c and e. Only the lamellar peak definition increased upon annealing (the full-width at half-maximum, FWHM) decreased, and the CCL increased (Table S5), indicating an improvement in the crystalline morphology. A similar observation was made for films processed with our optimized cosolvent system (o-xylene:tetralin 95:5 vol%) (Fig. 5d and f). However, for the cosolvent system, the crystallinity parameters of both lamellar and π–π stacking peaks also improved significantly upon annealing (Table S5). This result indicates that the morphology of the as-printed tetralin films was better than when using the cosolvent, but both morphologies became similar upon annealing. Furthermore, both solvent systems displayed no significant differences in crystallinity between the films annealed inside a glovebox and under vacuum (annealing right after IJP in our lab or onsite at ESRF). This observation suggests that the molecular arrangement did not
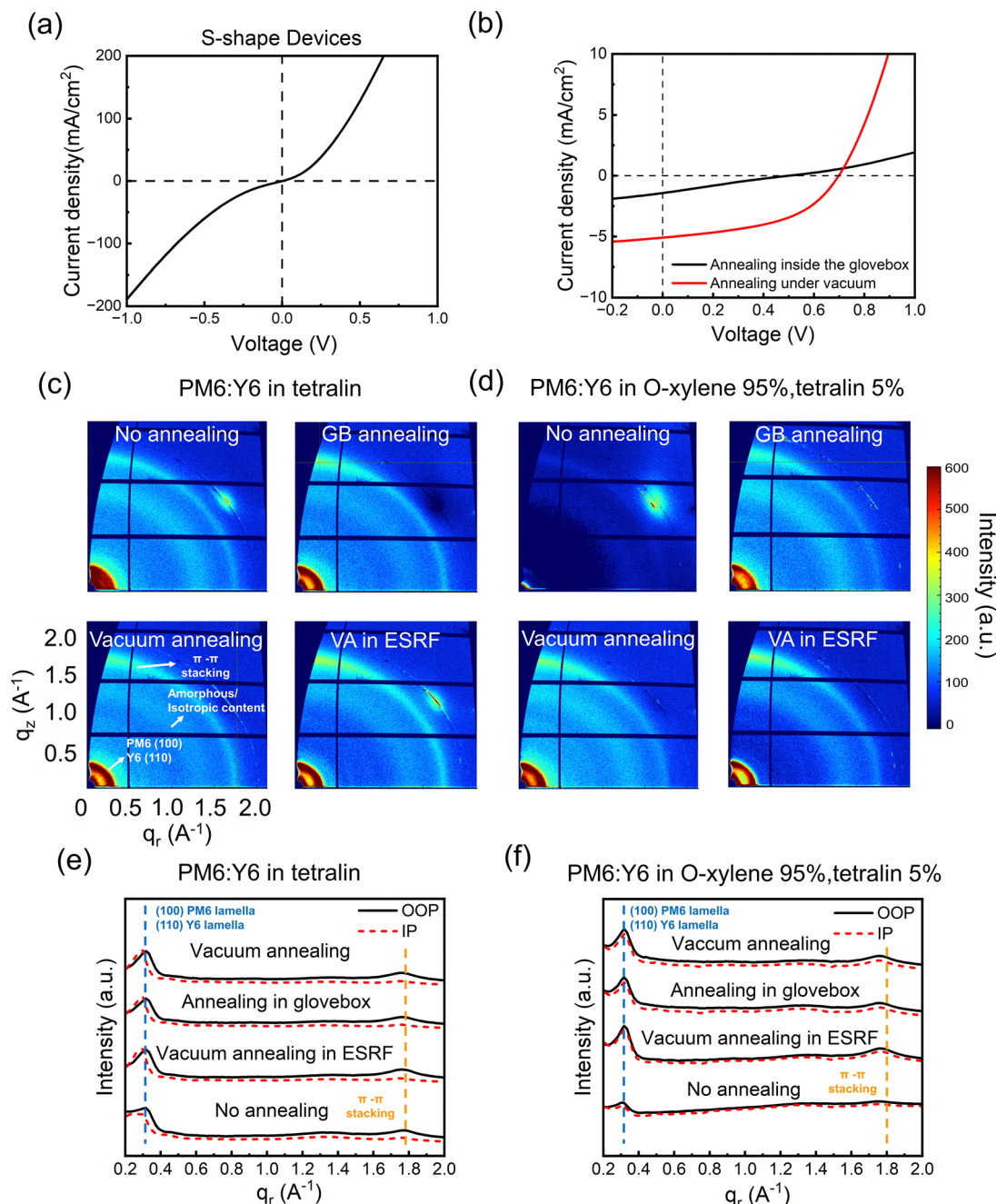
Fig. 5 Influence of thermal annealing on the structure–performance relationship of IJP PM6:Y6 blends. (a) Current density–voltage (*J–V*) curve of OPVs processed from tetralin and annealed at 140 °C for 30 minutes inside the glovebox according to the standard procedure for SC films. The curve shows an undesirable S-shape that crosses the origin. (b) Current density–voltage (*J–V*) curves of comparable OPVs annealed following approach (2) inside the glovebox for 60 min (black) and approach (3) under vacuum conditions for 30 min at 140 °C (red). 2D GIWAXS patterns of the blend film processed from (c) 100% tetralin and (d) 95 vol% *o*-xylene with 5 vol% tetralin. Corresponding 1D linecuts are shown in (e) and (f), respectively, under four different post-annealing conditions: no annealing, annealing inside the glovebox, annealing under vacuum conditions, and annealing under vacuum (on-site at ESRF).

depend on the annealing environment (glovebox or vacuum). Therefore, the increase in FF measured after vacuum annealing (Fig. 5b) must have arisen solely from the removal of entrapped solvent molecules in the active layer film. Those molecules likely induced charge trapping and could be eliminated with the use of vacuum annealing. SCLC measurements confirmed this hypothesis, showing that changing from annealing inside the glovebox to vacuum annealing led to a two orders of magnitude increase in electron mobility and one order in hole mobility (Table S2). Interestingly, despite the more favourable morphology of the as-printed tetralin films compared to the cosolvent films, and the similar morphology after annealing, the devices processed from tetralin displayed lower PCE than those processed from the cosolvent (Table S6). This observation

Table 2 Summary of PM6:Y6 OPVs fabricated and tested under different processing conditions, including variations in deposition method, thermal annealing, the use of 1-CN as an additive, and illumination conditions (1 sun or indoor light) for a device area of 0.04 cm². Four devices were characterized for the SC reference. For IJP devices, each reported value corresponds to the average performance of 10 devices across three independent batches. Reported errors are the standard errors of the mean

Deposition condition	Annealing condition	Additive 1-CN	Light condition	V_{oc} (V)	J_{sc} (mA cm^{-2})	FF (%)	PCE$_{avg}$ (%)	PCE$_{max}$ (%)
SC outside GB	Inside the glovebox	Without	1 sun	0.72	20.72	51	7.62 ± 0.22	8.20
SC inside GB	Inside the glovebox	Without	1 sun	0.79	22.41	70	12.37 ± 0.18	12.73
IJP	Inside the glovebox	Without	1 sun	0.56	4.01	35	0.88 ± 0.13	1.31
IJP	Vacuum annealing	Without	1 sun	0.65	6.59	48	2.05 ± 0.14	2.73
IJP	Vacuum annealing	Without	500 lux	0.29	0.02	40	1.6 ± 0.4	**4.37**
IJP	Vacuum annealing	With	1 sun	0.65	6.38	45	2.0 ± 0.3	3.31
IJP	Vacuum annealing	With	500 lux	0.35	0.02	42	1.8 ± 0.3	**3.74**

suggests that the vacuum annealing conditions tested were sufficient to remove small tetralin amounts (5 vol%) from the active layer processed from the cosolvent, but maybe not to remove large amounts from the films processed entirely from tetralin.

2.5. Performance under indoor light

As highly suited for smart wearables and other portable consumer electronics, we examined our IJP OPVs next under indoor conditions, i.e., an illumination of LED with 500 lux. Using the method described by Lübke et al.,[49] we calculated the indoor PCEs of our best devices (3 mg mL^{-1} processed from cosolvents o-xylene and tetralin, with thicknesses around 140 nm and vacuum annealed at 140 °C for 30 minutes) with and without 1-CN. Similar to what we encountered under 1-sun illumination, the device with 1-CN did not outperform the device without 1-CN under indoor illumination when considering the error of the measurements: the former showed a PCE$_{avg}$ of 1.8 ± 0.3%, and the latter 1.6 ± 0.4%. (Fig. S10 and Table 2). Interestingly, the devices without 1-CN measured under indoor illumination showed the highest PCE$_{max}$ measured in this work, 4.37%. This suggests that, contrary to what was concluded for 1-sun illumination, adding 1-CN does not hold promise for indoor applications. Regardless of the additive, the PCE$_{avg}$ of our IJP cells was comparable under indoor illumination and 1-sun, and the indoor PCE$_{max}$ surpassed that of the outdoor condition (Table 2). This finding is remarkable considering that PM6:Y6 is not a material system optimized to match the spectra of LED illumination. These results reveal the importance of tailoring the processing to the illumination conditions and highlight the potential of OPV for both outdoor and indoor applications.

3. Conclusions

In this study, we have performed a systematic investigation of the processing, design, and post-processing parameters involved in the fabrication of PM6:Y6 active layers for OPVs using a Fujifilm Dimatix® inkjet printer. Compared to the SC devices processed in chloroform outside the GB (PCE$_{max}$ = 7.62%), our best IJP OPVs using non-halogenated solvents (o-xylene:tetralin 95:5 vol%) fabricated under ambient

conditions achieved a PCE$_{max}$ of 3.31% under 1 sun illumination, and 4.37% under 500 lux LED light. Based on our observations, we propose the following general guidelines for the fabrication of IJP OPVs, which may also be extended to other similar systems:

3.1. Ink formulation

By introducing tetralin (a high-boiling-point, high-surface-tension solvent) into the primary solvent o-xylene (a low-boiling-point, low surface-tension solvent) as a cosolvent, the RMS surface roughness of the film was significantly reduced from 50.70 nm to 17.35 nm. This improvement is attributed to the suppression of the coffee-ring effect. Contrary to widely reported spin-coated OPVs, the advantages of adding 1-CN were not universal. At 1 sun illumination, 1-CN showed potential to achieve higher PCE$_{max}$ values. This potential was underpinned by morphological changes (inferred by AFM and GIWAXS analysis) that translated into decreasing the R_s from 90 Ω cm² to 2.05 Ω cm², and increasing both electron and hole mobilities by an order of magnitude (SCLC study). This increase in PCE$_{max}$ came at the expense of a larger spread in the measurements, suggesting a less reproducible process upon adding 1-CN. The potential advantage introduced by 1-CN to reach high PCEs was reversed for indoor illumination.

3.2. Processing parameters

An M-shaped waveform, with a moderate amplitude in the second part, enabled the efficient ejection of optimal droplets for highly concentrated inks without generating satellite droplets. During the IJP process, the frequency of 10 kHz, three nozzles, and a DS of 20 μm were chosen to form continuous films without pinholes or wavy edges based on fiducial camera images. These parameters determined the drying behaviour and morphology of the IJP film. The number of printed layers was adjusted according to the R_s and R_{sh} values of the devices. With an optimal film thickness of approximately 140 nm, the lowest R_s of 4.9 Ω cm² and the highest R_{sh} of 4.70 × 10⁹ Ω cm² were achieved. The optimal substrate plate temperature was then determined to be 60 °C based on GIWAXS crystallinity, which showed that at high plate temperature, PM6:Y6 blend films exhibited a moderate increase in both IP lamellar

ordering and π–π stacking crystallinity, primarily driven by the enhanced crystallinity of PM6.

3.3. Thermal annealing conditions

In order to mitigate the short-circuited S-shaped J–V curves, post-annealing of the active layer under vacuum was found to be the most effective approach, leading to an improvement in PCE. Compared to annealing conducted inside the glovebox, vacuum annealing removed residual solvents more efficiently without degrading the active layer material, as the boiling point of tetralin decreased from 207 °C at ambient pressure to ∼97.5 °C at 10 mmHg. GIWAXS analysis showed that the CCL increased upon thermal annealing compared to the as-cast films. However, differences in CCL among the various annealing environments (glovebox and vacuum) were relatively minor. The enhancement in PCE under vacuum annealing can therefore be attributed primarily to the increased charge carrier mobility associated with less charge trapping by solvent residue, as confirmed by SCLC measurements: the electron mobility increased by nearly two orders of magnitude, while the hole mobility increased by approximately one order.

3.4. Illumination under 1 sun and indoor light

Even though PM6:Y6 is not optimized for indoor conditions, the maximum PCE of our IJP active layer was higher for indoor LED 500 lux light than under 1 sun illumination: PCE_{max} = 4.37% vs. 3.31%. It is also worth noting that for a certain material, the optimal processing conditions might be different for indoor and outdoor operation. In this case, adding 1-CN helped PCE_{max} only under 1 sun.

Among the four categories mentioned in this work, the post-processing (vacuum) thermal annealing was the most important as it fixed short-circuited devices by effectively removing high-boiling point solvent residue and increasing the FF and J_{sc}. These insights will help to develop the next generation of low-cost organic indoor devices for IoT applications and portable consumer electronics.

4. Experimental section

4.1. Materials and ink formulation

Patterned ITO on glass substrates were purchased from BIO-TAIN CRYSTAL CO., LIMITED. ZnO nanoparticles (ZnO NP) dispersion (N-12) was purchased from Avantama with 5 wt% ZnO in ethanol. Diluted ZnO ink was formulated with ZnO NP:ethanol = 1:1.25. Active layer: PM6 (M2150A12) and Y6 were purchased from Ossila. For inkjet printing, 3 mg mL^{-1} PM6:Y6 with the ratio of 1:1.2, and 0.5 wt% 1-chloronaphthalene (1-CN) (Sigma Aldrich) solution were dissolved in the mixture solution of o-xylene 95% v/v (Alfa Aesar) and anhydrous tetralin 5% v/v (Sigma Aldrich). The prepared solution was stirred for at least 4 h and was filled into the Samba® cartridge LCP fluid module through a GF/PET 0.45 μm-pore size syringe filter. The cartridge module was then inserted into a vacuum chamber to degas for 30 min to avoid the formation of bubbles inside the fluid.

4.2. Organic solar cell fabrication

Organic solar cell devices were fabricated with the inverted structure: glass (1 mm)/ITO (135 nm)/ZnO (30 nm)/PM6:Y6 (0.5% CN) (140 nm)/MoO$_3$ (14 nm)/Ag (100 nm). The ITO patterned glass substrates were cleaned with detergent for 15 min, 3 times with deionized water for 10 min each, acetone for 15 min, isopropyl alcohol for 15 min, and finally dried with nitrogen. Ozone plasma for 30 min was used to increase the substrates' wettability. Subsequently, the prepared ETL solution was deposited by spin-coating diluted ZnO at 3000 rpm for 20 s, followed by annealing in ambient conditions at 100 °C for 10 min to form approximately a 30 nm film. Active layers were fabricated by either spin-coating or inkjet printing with DMP-2850 inkjet printer and Samba® cartridge modules (2.4 pL) with 12 nozzles (out of which, 3 adjacent ones were selected for printing). The spin-coated film was fabricated by dissolving the PM6:Y6 blend (1:1.2 by weight) in chloroform and spin-coating through a GF/PET filter with pore size 0.45 mm at 2500 rpm for 60 s, yielding a nominal thickness of 140 nm, followed by post-annealing at 120 °C for 15 min. For the inkjet printed active layer film, we optimized the drop-to-drop spacing (DS) to 15–20 mm and printed the film under ambient conditions. Following fabrication, all devices were annealed either in the glovebox or under vacuum on a vacuum hot plate (J.P. Selecta Vacuo-Temp). MoO$_3$ (14 nm) and Ag (100 nm) were evaporated at UHasselt IMO-IMOMEC. All the devices mentioned had an active area of 0.04 cm^2. Samples for GIWAXS measurements were annealed in our lab, vacuum-sealed inside the glovebox, and transported to ESRF (Grenoble). A few samples were annealed on-site using a vacuum hot plate available in a lab next to the beamline (BM26) hutch.

4.3. Measurements

The current density–voltage (J–V) characteristics of the devices were measured under 1 sun conditions with an AM 1.5 solar simulator (Newport 91195A) and irradiation intensity of 100 mW cm^{-2} using a Keithley 2360. The light intensity was calibrated with a Si reference cell. The devices were measured right after the thermal evaporation of Ag in the glove box. The voltage sweep was from −1 V to 1 V with a 0.02 V step.

GIWAXS measurements were performed at the BM26 beamline (DUBBLE) of the European Synchrotron Radiation Facility (ESRF) at Grenoble (France). Samples were irradiated with X-rays at an energy of 13.346 keV. The sample-to-detector distance (328.841 mm) was calibrated, and the incident angle was fixed at 0.12°. In our experiment, the accumulation time was fixed at 30 s. To reduce air scattering, a helium-filled flight tube was placed between the sample and the detector. 2D GIWAXS patterns were collected using a Pilatus 1 M detector and visualized using GIuSAXS, a software tool developed by DUBBLE@ESRF. 1D Data extraction was carried out with GIXS-GUI, which was used to obtain both the sample and the background signals. 1D linecuts were subsequently generated by subtracting the background from the sample signal. To determine other parameters of interest from the GIWAXS patterns

(1D linecuts), a fitting procedure was followed using Python. Initially, an Asymmetric Least Squares (ASLS) procedure was used to estimate a baseline for each data set, which was subsequently subtracted from intensity values. Following this baseline correction, peaks were identified with an in-built peak-finding algorithm, followed by the fitting of Gaussian curves to each of these peaks. From the curve fitting results, the precise peak position, peak intensity, full-width at half-maximum (FWHM = 2.355 × standard deviation), and the area under the curves were extracted. Subsequently, the crystalline coherence length (CCL) was calculated using the Scherrer equation (eqn (1)). The shape factor K was set to 0.9, a value commonly adopted in the literature for polymer:non-fullerene blend films.

$$CCL = \frac{2\pi K}{FWHM} \qquad (1)$$

4.3.1. AFM measurement. The thickness value and the phase separation images of the active layer were obtained by NaioAFM. A scanning speed of 1 s and a setpoint value between 50% to 70% were chosen for optimal imaging. Further thickness and RMS surface roughness characterizations were performed using the software Gwyddion.

4.3.2. SCLC device structure and characterization. The hole-only device structure was: ITO (135 nm)/PEDOT:PSS (20 nm)/PM6:Y6 (140 nm)/MoO_3 (14 nm)/Ag (100 nm). The electron-only device structure was: ITO (135 nm)/ZnO (30 nm)/PM6:Y6 (140 nm)/Ca (20 nm)/Al (80 nm). The voltage sweep was from 0 V to 3 V with a 0.03 V step. Within this scanning regime, the current transport is governed by the space-charge-limited current (SCLC) model where J–V characteristics follow a quadratic dependence ($J \propto V^2$) given by the Mott–Gurney equation,

$$J = (9/8)\varepsilon_r\varepsilon_0\mu V^2/L^3 \qquad (2)$$

where J is the current density, ε_r is the relative permittivity (≈ 3–4 for organic material), ε_0 is the vacuum permittivity, μ is the charge carrier mobility, V is the applied voltage, and L is the active layer thickness.

Conflicts of interest

There are no conflicts to declare.

Data availability

Data for this article, including I–V measurements and other characterisation data, are available at KU Leuven RDR at https://doi.org/10.48804/RTXOUS.

The following data and descriptions of procedures supporting this work can be found in the supplementary information: fiducial camera images to optimize printing conditions, the 1-diode model, SCLC data, optical images of OPV cells with residual solvent in the active layer, AFM profiles, thermal protocol details, extra J–V curves, estimation of tetralin boiling point using the Clausius–Clapeyron equation, GIWAXS fitting data. See DOI: https://doi.org/10.1039/d5ma01033k.

References

1 H. Lee, S. Jeong, J. H. Kim, Y. R. Jo, H. J. Eun, B. Park, S. C. Yoon, J. H. Kim, S. H. Lee and S. Park, *npj Flexible Electron.*, 2023, **7**, 27, DOI: **10.1038/s41528-023-00260-5**.

2 N. Espinosa, F. O. Lenzmann, S. Ryley, D. Angmo, M. Hösel, R. R. Søndergaard, D. Huss, S. Dafinger, S. Gritsch, J. M. Kroon, M. Jørgensen and F. C. Krebs, *J. Mater. Chem. A*, 2013, **1**, 7037–7049, DOI: **10.1039/c3ta01611k**.

3 T. Xu, Y. Luo, S. Wu, B. Deng, S. Chen, Y. Zhong, S. Wang, G. Lévêque, R. Bachelot and F. Zhu, *Adv. Sci.*, 2022, **9**, 2202150, DOI: **10.1002/advs.202202150**.

4 H. Chen, Y. Huang, R. Zhang, H. Mou, J. Ding, J. Zhou, Z. Wang, H. Li, W. Chen, J. Zhu, Q. Cheng, H. Gu, X. Wu, T. Zhang, Y. Wang, H. Zhu, Z. Xie, F. Gao, Y. Li and Y. Li, *Nat. Mater.*, 2025, **24**, 444, DOI: **10.1038/s41563-024-02062-0**.

5 R. S. Gurney, D. G. Lidzey and T. Wang, *Rep. Prog. Phys.*, 2019, **82**, 036601, DOI: **10.1088/1361-6633/ab0530**.

6 C. Yan, S. Barlow, Z. Wang, H. Yan, A. K. Y. Jen, S. R. Marder and X. Zhan, *Nat. Rev. Mater.*, 2018, **3**, 18003, DOI: **10.1038/natrevmats.2018.3**.

7 L. K. Ma, Y. Chen, P. C. Y. Chow, G. Zhang, J. Huang, C. Ma, J. Zhang, H. Yin, A. M. Hong Cheung, K. S. Wong, S. K. So and H. Yan, *Joule*, 2020, **4**, 1486–1500.

8 T. H. Kim, N. W. Park, M. A. Saeed, S. Y. Jeong, H. Y. Woo, J. H. Park and J. W. Shim, *Nano Energy*, 2023, **112**, 108429, DOI: **10.1016/j.nanoen.2023.108429**.

9 J. Yuan, Y. Zhang, L. Zhou, G. Zhang, H. L. Yip, T. K. Lau, X. Lu, C. Zhu, H. Peng, P. A. Johnson, M. Leclerc, Y. Cao, J. Ulanski, Y. Li and Y. Zou, *Joule*, 2019, **3**, 1140–1151.

10 S. Shoaee, H. M. Luong, J. Song, Y. Zou, T. Q. Nguyen and D. Neher, *Adv. Mater.*, 2024, **36**, 2302005, DOI: **10.1002/adma.202302005**.

11 X. Jiang, B. Siegmund and K. Vandewal, *Mater. Horiz.*, 2024, **11**, 3903–3910.

12 S. Dong, T. Jia, K. Zhang, J. Jing and F. Huang, *Joule*, 2020, **4**, 2004–2016.

13 G. Yao, Y. Ge, X. Xiao, L. Zhang, N. Yi, H. Luo, S. Yuan and W. Zhou, *ACS Appl. Energy Mater.*, 2022, **5**, 1193–1204.

14 G. J. N. Wang, F. Molina-Lopez, H. Zhang, J. Xu, H. C. Wu, J. Lopez, L. Shaw, J. Mun, Q. Zhang, S. Wang, A. Ehrlich and Z. Bao, *Macromolecules*, 2018, **51**, 4976–4985.

15 C. Liu, J. Liu, X. Duan and Y. Sun, *Adv. Sci.*, 2023, **10**, 2303842, DOI: 10.1002/advs.202303842.

16 D. Corzo, D. Rosas-Villalva, C. Amruth, G. Tostado-Blázquez, E. B. Alexandre, L. H. Hernandez, J. Han, H. Xu, M. Babics, S. De Wolf and D. Baran, *Nat. Energy*, 2023, **8**, 62–73.

17 C. N. Hoth, S. A. Choulis, P. Schilinsky and C. J. Brabec, *Adv. Mater.*, 2007, **19**, 3973–3978.

18 S. Jung, A. Sou, K. Banger, D. H. Ko, P. C. Y. Chow, C. R. McNeill and H. Sirringhaus, *Adv. Energy Mater.*, 2014, **4**, 1400432, DOI: 10.1002/aenm.201400432.

19 T. M. Eggenhuisen, Y. Galagan, A. F. K. V. Biezemans, T. M. W. L. Slaats, W. P. Voorthuijzen, S. Kommeren, S. Shanmugam, J. P. Teunissen, A. Hadipour, W. J. H. Verhees, S. C. Veenstra, M. J. J. Coenen, J. Gilot, R. Andriessen and W. A. Groen, *J. Mater. Chem. A*, 2015, **3**, 7255–7262.

20 E. Bihar, D. Corzo, T. C. Hidalgo, D. Rosas-Villalva, K. N. Salama, S. Inal and D. Baran, *Adv. Mater. Technol.*, 2020, **5**, 2000226, DOI: 10.1002/admt.202000226.

21 P. Perkhun, W. Köntges, F. Pourcin, D. Esteoulle, E. Barulina, N. Yoshimoto, P. Pierron, O. Margeat, C. Videlot-Ackermann, A. K. Bharwal, D. Duché, C. R. Herrero, C. Gonzales, A. Guerrero, J. Bisquert, R. R. Schröder, M. Pfannmöller, S. Ben Dkhil, J.-J. Simon and J. Ackermann, *Adv. Energy Sustainability Res.*, 2021, **2**, 2000086.

22 K. C. Tam, P. Kubis, P. Maisch, C. J. Brabec and H. J. Egelhaaf, *Prog. Photovoltaics Res. Appl.*, 2022, **30**, 528–542.

23 M. Steinberger, A. Distler, J. Hörber, K. C. Tam, C. J. Brabec and H. J. Egelhaaf, *Flexible Printed Electron.*, 2024, **9**, 025018, DOI: 10.1088/2058-8585/ad50e7.

24 X. Chen, R. Huang, Y. Han, W. Zha, J. Fang, J. Lin, Q. Luo, Z. Chen and C. Q. Ma, *Adv. Energy Mater.*, 2022, **12**, 2200044, DOI: 10.1002/aenm.202200044.

25 W. Wang, Y. W. Su and C. H. Chang, *Sol. Energy Mater. Sol. Cells*, 2011, **95**, 2616–2620.

26 M. Wang, X. Cai, Y. Huang, K. Zheng and F. Li, *Front. Phys.*, 2020, **8**, 578317, DOI: 10.3389/fphy.2020.578317.

27 V. I. Madogni, B. Kounouhéwa, A. Akpo, M. Agbomahéna, S. A. Hounkpatin and C. N. Awanou, *Chem. Phys. Lett.*, 2015, **640**, 201–214.

28 W. R. Mateker and M. D. McGehee, *Adv Mater*, 2017, **29**, 1603940, DOI: 10.1002/adma.201603940.

29 T. P. A. van der Pol, B. T. van Gorkom, W. F. M. van Geel, J. Littmann, M. M. Wienk and R. A. J. Janssen, *Adv. Energy Mater.*, 2023, **13**, 2300003, DOI: 10.1002/aenm.202300003.

30 D. Corzo, E. Bihar, E. B. Alexandre, D. Rosas-Villalva and D. Baran, *Adv. Funct. Mater.*, 2021, **31**, 2005763, DOI: 10.1002/adfm.202005763.

31 R. Sliz, J. Czajkowski and T. Fabritius, *Langmuir*, 2020, **36**, 9562–9570.

32 G. Hu, L. Yang, Z. Yang, Y. Wang, X. Jin, J. Dai, Q. Wu, S. Liu, X. Zhu, X. Wang, T. C. Wu, R. C. T. Howe, T. Albrow-Owen, L. W. T. Ng, Q. Yang, L. G. Occhipinti, R. I. Woodward, E. J. R. Kelleher, Z. Sun, X. Huang, M. Zhang, C. D. Bain and T. Hasan, *Sci. Adv.*, 2020, **6**(33), DOI: 10.1126/sciadv.aba5029.

33 D. H. Lee, D. H. Kim, T. Kim, D. C. Lee, S. Cho and T. Park, *Nano Energy*, 2022, **93**, 106878, DOI: 10.1016/j.nanoen.2021.106878.

34 W. De Soto, S. A. Klein and W. A. Beckman, *Sol. Energy*, 2006, **80**, 78–88.

35 L. Zhu, M. Zhang, G. Zhou, T. Hao, J. Xu, J. Wang, C. Qiu, N. Prine, J. Ali, W. Feng, X. Gu, Z. Ma, Z. Tang, H. Zhu, L. Ying, Y. Zhang and F. Liu, *Adv. Energy Mater.*, 2020, **10**, 1904234, DOI: 10.1002/aenm.201904234.

36 X. Wang, C. Feng, P. Liu, Z. He and Y. Cao, *Small*, 2022, **18**, 2107106, DOI: 10.1002/smll.202107106.

37 X. Gu, H. Yan, T. Kurosawa, B. C. Schroeder, K. L. Gu, Y. Zhou, J. W. F. To, S. D. Oosterhout, V. Savikhin, F. Molina-Lopez, C. J. Tassone, S. C. B. Mannsfeld, C. Wang, M. F. Toney and Z. Bao, *Adv. Energy Mater.*, 2016, **6**, 1601225, DOI: 10.1002/aenm.201601225.

38 S. Alam, H. Aldosari, C. E. Petoukhoff, T. Váry, W. Althobaiti, M. Alqurashi, H. Tang, J. I. Khan, V. Nádaždy, P. Müller-Buschbaum, G. C. Welch and F. Laquai, *Adv. Funct. Mater.*, 2024, **34**, 2308076, DOI: 10.1002/adfm.202308076.

39 F. Molina-Lopez, T. Z. Gao, U. Kraft, C. Zhu, T. Öhlund, R. Pfattner, V. R. Feig, Y. Kim, S. Wang, Y. Yun and Z. Bao, *Nat. Commun.*, 2019, **10**, 2676, DOI: 10.1038/s41467-019-10569-3.

40 H. Y. Gan, X. Shan, T. Eriksson, B. K. Lok and Y. C. Lam, *J. Micromech. Microeng.*, 2009, **19**, 055010, DOI: 10.1088/0960-1317/19/5/055010.

41 D. Soltman and V. Subramanian, *Langmuir*, 2008, **24**, 2224–2231.

42 J. Perelaer, PhD thesis, Eindhoven University of Technology, 2009.

43 J. F. Salmerón, F. Molina-Lopez, D. Briand, J. J. Ruan, A. Rivadeneyra, M. A. Carvajal, L. F. Capitán-Vallvey, N. F. De Rooij and A. J. Palma, *J. Electron. Mater.*, 2014, **43**, 604–617.

44 Y. Xiao, J. Yuan, G. Zhou, K. C. Ngan, X. Xia, J. Zhu, Y. Zou, N. Zhao, X. Zhan and X. Lu, *J. Mater. Chem. A*, 2021, **9**, 17030–17038.

45 B. Reyes-Suárez, Z. Du, N. Thomas, Z.-Z. Qu, T. Pawlak, R. Vasant, D. Vu, S. Yoon, S. Mugiraneza, Y. Lai, J. Fishburn, S. Chae, A. Yi, P. Raval, S. Mukherjee, Y. Qin, S. Xiao, H. Kim, H. Ade, T.-Q. Nguyen and G. N. M. Reddy, *ACS Energy Lett.*, 2025, DOI: 10.1021/acsenergylett.5c01692.

46 L. Zuo, J. Yao, H. Li and H. Chen, *Sol. Energy Mater. Sol. Cells*, 2014, **122**, 88–93.

47 K. Tada, *Mol. Cryst. Liq. Cryst.*, 2017, **653**, 39–43.

48 F. García-Sánchez, B. Romero, D. Lugo-Muñoz, P. Del, B. Arredondo, J. Liou and A. Ortiz-Conde, *Facta Univ., Electron. Energ.*, 2017, **30**, 327–350.

49 D. Lübke, P. Hartnagel, J. Angona and T. Kirchartz, *Adv. Energy Mater.*, 2021, **11**, 2101474, DOI: 10.1002/aenm.202101474.